Identification of elasto-plastic and nonlinear fracture mechanics parameters of silver-plated copper busbars for photovoltaics

Identification of elasto-plastic and nonlinear fracture mechanics parameters of silver-plated copper busbars for photovoltaics

V. Carollo[a], D. Piga[b], C. Borri[a], M. Paggi[a,*]

[a] *IMT School for Advanced Studies Lucca, Piazza San Francesco 19, 55100 Lucca, Italy*
[b] *Dalle Molle Institute for Artificial Intelligence - USI/SUPSI, Galleria 2, Via Cantonale 2c, CH-6928 Manno, Switzerland*

Abstract

Silver-plated copper busbars are screen printed onto silicon solar cells and have the key role to collect the electric current produced by the solar cell. Busbars of two adjacent solar cells are then connected by a soldered ribbon made of the same material. Due to mechanical and thermal loads, such a ribbon is subject to axial deformation that, often, causes plasticity and, in some cases, its breakage due to crack growth. A procedure based on the gradient-descent method and particle swarm optimization is herein proposed for the identification of elasto-plastic and nonlinear (cohesive zone model, CZM) fracture mechanics parameters of silver-plated copper busbars. The proposed method requires the experimental determination of the force-displacement curves from uniaxial tensile tests on busbar samples with and without initial notches. The inspection of in situ SEM images during the tests allows also the estimation of the crack opening, which is found to be an important local quantity to assess the reliability of different CZMs in simulating a crack growth process consistent with the real one.

Keywords: Cohesive zone model; elasto-plastic fracture; parameters identification; gradient descent method; particle swarm optimization.

*Corresponding author
Email address: marco.paggi@imtlucca.it (M. Paggi)

Nomenclature

a_0: initial notch length;
E: Young modulus;
g_{c}: critical crack opening for complete decohesion;
$g_{\max}$: crack opening corresponding to the peak CZM traction;
g_{n}: crack opening;
h: number defining a given far-field imposed displacement;
H: hardening coefficient;
K: initial stiffness of the ascending branch of the bilinear CZM;
N: total number of far-field imposed displacements;
$\mathbf{p}$: vector of model parameters to the identified;
$\mathbf{p}^{\mathrm{opt}}$: identified (optimal) vector of model parameters;
q_{h}: positive weights;
α, β: backtracking line search parameters;
Φ: objective (cost) function to be minimized;
σ: Mode I cohesive traction;
$\sigma_{\max}$: peak cohesive traction;
σ_{y}: yield stress;
CZM: cohesive zone model;
PSO: particle swarm optimization;
SEM: scanning electron microscope;
SEM: scanning electron microscope.

1. Introduction

Busbars are screen printed onto silicon solar cells and have the key role to collect the electric current produced by the solar cell from the incoming photons, see Fig1(a). Busbars of two adjacent solar cells are connected by a soldered ribbon, see Fig. 1(b), made of the same material and a tiny free space is left between the solar cells, which are then encapsulated into a photovoltaic (PV) laminate [1]. Busbars and the electric ribbon are made of copper coated by silver, in order to maximize their electric conductivity and reduce resistance losses.

Due to mechanical and thermal loads, the connecting ribbon is subject to axial deformation. For instance, the gap between two solar cells, usually 2 mm wide at room temperature, has been measured in [2, 3] to have an increase of 60 μm at a temperature $T = 80°$C, due to thermo-elastic deformation of the materials. As

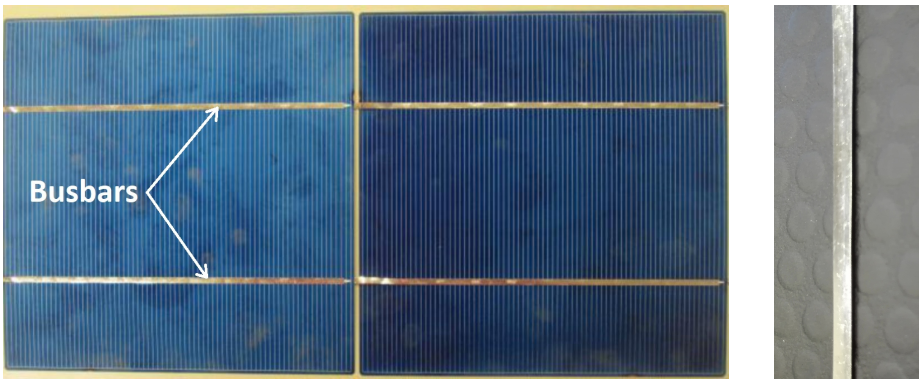

(a) Two solar cells connected by busbars (b) Busbar

Figure 1: (a) busbars used to electrically connect solar cells; (b) detail of the busbar.

experimentally found in [4], the strain level for the activation of plasticity in busbars is about 0.001, which is about one order of magnitude smaller than the axial strain induced by thermo-elastic deformation in the field. In some cases, due to tiny defects introduced by soldering of the ribbon onto the busbars, interconnect breakage is a failure mechanism sometimes observed in PV operations [5], very important because it can lead to hot spots and severe PV laminate damage. So far, research on the mechanical behavior of busbars has mainly focused on the prediction of their deformation in the linear elastic regime, while there is a lack of a complete characterization of their response in the presence of plasticity and fracture.

Based on these premises, we herein extend in this study the investigation in [4] by considering the interplay of plasticity and nonlinear crack growth in busbar specimens under tension, examining also notched specimens with crack growth in pure Mode I, in addition to unnotched specimens. We restrict the issue of parameters identification for the two constitutive models herein used to depict the material nonlinearities to monotonic loading conditions and pure Mode I crack growth. This is motivated by the fact that a reduced number of material parameters can be identified as compared to a more general non-monotonic loading history, or in the presence of a more complex Mixed-Mode crack propagation. To elucidate on these topics left for further research, the complexities arising due to cyclic loading are finally addressed in the discussion and conclusion section.

It has to be emphasized that the problem of nonlinear crack growth in elasto-plastic materials is a complex research topic due to the simultaneous presence of two forms of mechanical nonlinearities, *i.e.*, elasto-plasticity, which leads to energy dissipation in the bulk, and crack growth, which leads to energy dissipation due to the formation of a stress-free surface. In order to provide a computational model able to simulate the behaviour of busbars in realistic conditions and assess possible failure scenarios, useful for the design of novel multi-busbar solar cell architectures, it is therefore necessary to identify all the constitutive model parameters for elasto-plasticity and nonlinear fracture mechanics.

In this work, we propose a combined experimental-computational procedure based on the gradient-descent method and particle swarm optimization, two classical identification approaches available in the literature, for the challenging identification of elasto-plastic and CZM fracture mechanics parameters of silver-plated copper busbars. To this aim, the experimental determination of the force-displacement curves from uniaxial tensile tests on busbar samples with and without initial notches is requested, as discussed in Sec. 2. It will be also shown that the inspection of in situ images acquired with a scanning electron microscope (SEM) during the tests, albeit not necessary for parameters identification, is however very important to estimate local fracture quantities such as the crack opening, and judge about the reliability of different identified CZMs in simulating crack growth. Section 3 provides a short overview of the nonlinear material models for elasto-plasticity and nonlinear fracture mechanics herein considered. In particular, two different CZMs are examined, to compare the complexities in their parameters' identification and also assess the role played by their shape in simulating the fracture process. Section 4 discusses the nonlinear optimization algorithms proposed and presents the results of model parameters' identification, with a discussion on the convergence of each method. Other alternative idntification strategies available in the literature are also discussed in relation to their possible generalization and application to the present problem. Finally, discussion and conclusion complete the article, illustrating also future perspectives of research.

2. Experimental tests on busbars

The experimental campaign described in this section has been conducted in the MUSAM-Lab of the IMT School for Advanced Studied Lucca. In-situ uniaxial tensile tests on unnotched and notched speciments have been performed by using the Deben Gatan MTEST5000S tensile stage (Fig. 2). The stage is located inside the Zeiss EVO MA15 scanning electron microscope (SEM), capable of working with variable pressure to avoid metallization or graphitization of the sample surface. For each level of the imposed axial displacement, controlled by the tensile stage, the reaction force is measured by the loading cell. Displacement control can also allow for cyclic axial tests. In addition to force-displacement diagrams, microscopy images of the deformed specimen surface can be acquired using the SEM. This allows the observation of the evolution of crack propagation, the assessment of the amount of crack opening along the crack flanks, providing micromechanical information on the local deformation process near the crack-tip.

Busbar specimens have a free span of 17 mm, a width of 2.6 mm, and a thickness of 0.2 mm. They are clamped on both sides, by introducing a thin layer of teflon to avoid local failure modes near the steel platens. The acquisition of SEM images showed that all the recorded displacements were compatible with material deformation only, without any component associated to rigid body motion, thus excluding slippage of the specimens from clamps. In addition to unnotched specimens (Fig. 3(a)) notched specimens with a notch size $a_0 = 0.45$ and 0.80 mm have been considered, see Figs.3(b) and 3(c). Notches have been made

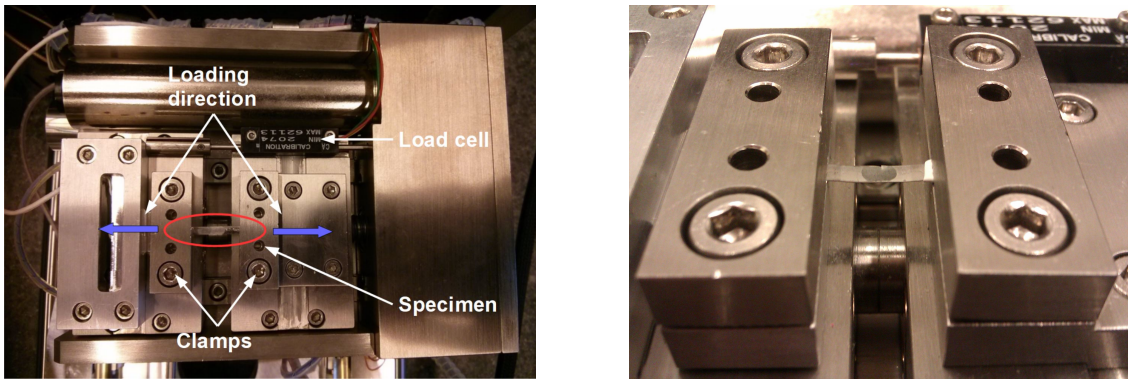

(a) Tensile stage (b) Detail of the clamped specimen

Figure 2: Tensile stage: (a) experimental setup; (b) detail of the clamped specimen.

using scissors under an optical microscope. SEM measurements have shown that this manual method was leading to cuts whose lengths were equal to 0.45±0.01 mm and 0.80±0.01 mm for the two notch sizes, respectively. Tests have been performed by applying a monotonically increasing uniaxial displacement Δ up to failure, with a constant rate of 0.033 mm/min to achieve quasi-static conditions. To assess the amount of scattering in the experimental data, 10 specimens for each geometry have been tested under the same conditions.

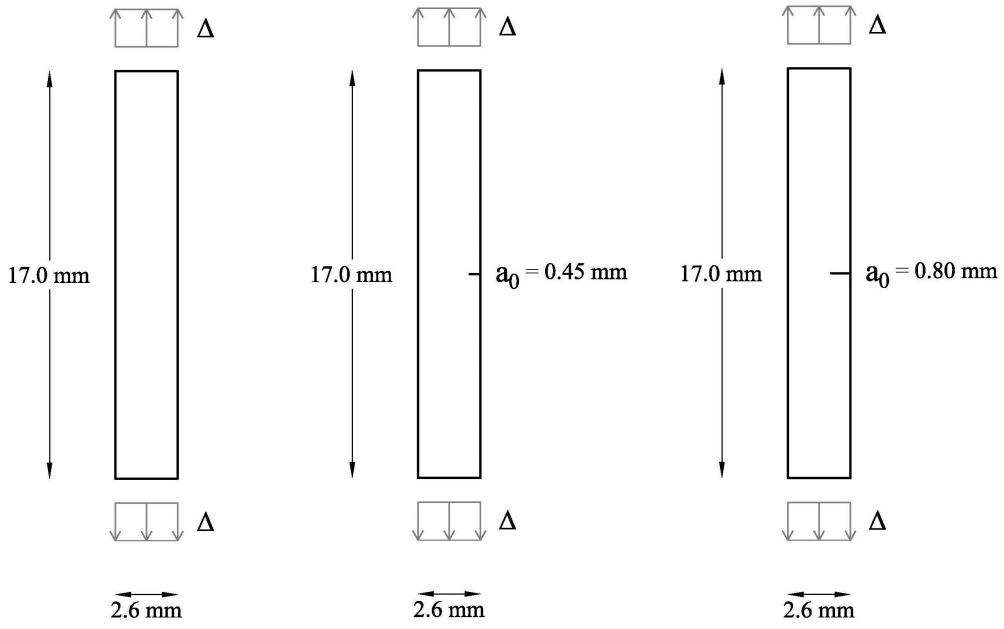

(a) Unnotched (b) Notched ($a_0 = 0.45$ mm) (c) Notched ($a_0 = 0.80$ mm)

Figure 3: Geometry of the different unnotched and notched busbar specimens tested under uniaxial tension.

Fig. 4 shows the typical results of the unaxial tensile tests in terms of force-displacement curves. The

small drops in the force levels are caused by material relaxation every time the imposed displacement is hold for a short period required to record surface images with SEM. The curve corresponding to the unnotched specimen suggests a typical behaviour of an elasto-plastic material characterized by a linear regime followed by hardening. The curves corresponding to notched specimens have very different trends due to the coupled action of plasticity and crack growth. The first part of the curves is linear with a slope that is a decreasing function of the initial notch size. Afterwards, by increasing the applied displacement, SEM images show blunting of the notch as a typical consequence of plasticity (see e.g. Figs. 5(a) and 5(b) corresponding to the 0.45 notched specimen). A further increase in the tensile displacement leads to the propagation of a sharp crack from the notch tip (see Figs. 5(c)-(f)), which is responsible for the progressive softening in the force-displacement curve. The crack path at failure is shown in Fig. 6. Therefore, for notched specimens, we can distinguish between a linear elastic regime (1), a plastic-dominant regime (2), and a plastic & fracture regime (3), see, as an example, the labels in blue in Fig. 4 for the notched specimen with $a_0 = 0.80$ mm.

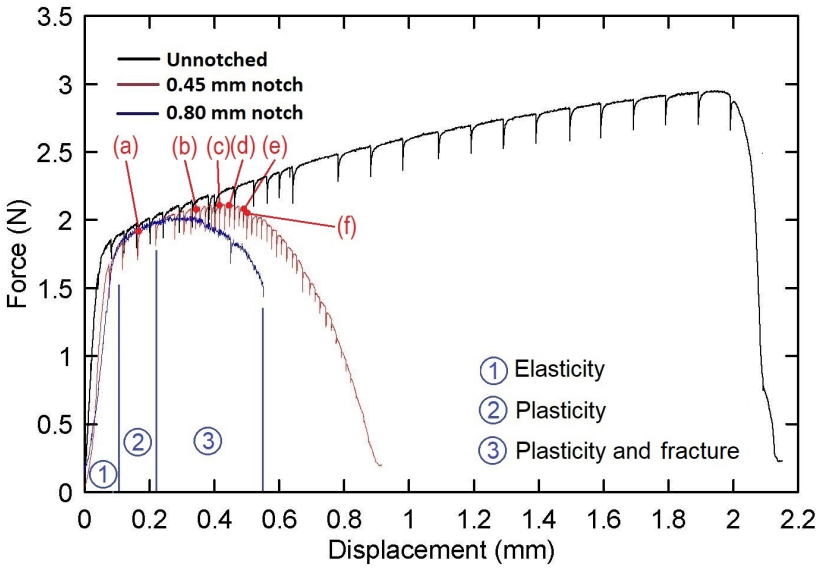

Figure 4: Force-displacement curves of the tested specimens: unnotched specimen, 0.45-mm notched specimen, and 0.80-mm notched specimen. Red labels refer to the sequence of SEM images in Fig. 5.

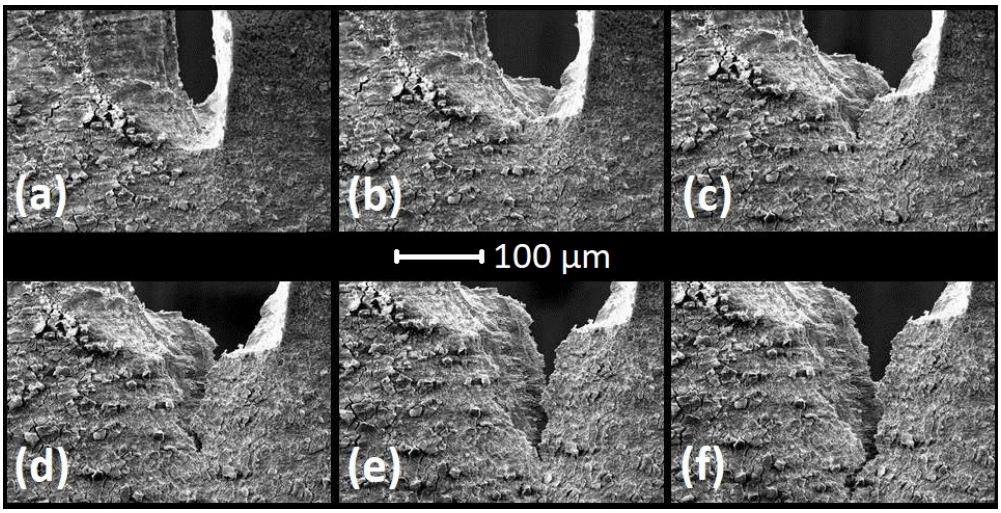

Figure 5: Evolution of the notch tip deformation during the tensile test of the 0.45 mm notched specimen. For each image, the value of the far-field imposed displacement is: (a) 0.163 mm; (b) 0.340 mm; (c) 0.415 mm; (d) 0.445 mm; (e) 0.490 mm; (f) 0.500 mm.

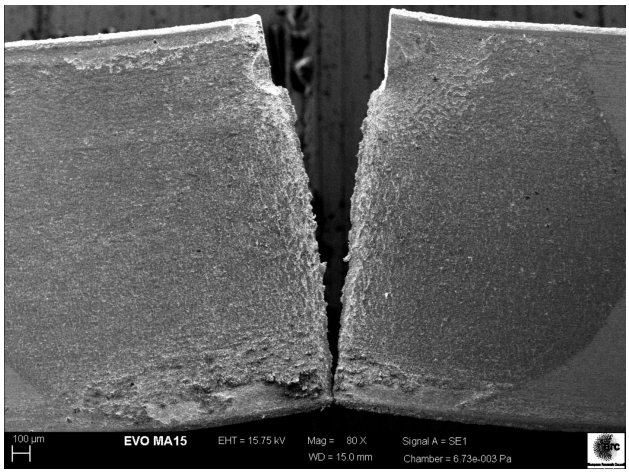

Figure 6: Crack path at failure of the specimen with $a_0 = 0.45$ mm notch size.

3. Material models

Different material models have to be considered for the simulation of the nonlinear behaviour of busbars. Plasticity in the bulk can be mathematically described by a von Mises elasto-plastic constitutive material model with linear hardening. The corresponding material parameters to be identified are the Young's modulus E, the yield stress σ_y, and the hardening coefficient H.

To model surface energy dissipation associated to crack propagation, on the other hand, cohesive zone fracture models (CZMs) have to be introduced to predict the nonlinear process of crack growth. Here, we examine two options for the relation between the Mode I cohesive traction and its energetically associated crack opening displacement g_{n}. The former is a polynomial CZM proposed in [6] and graphically shown in

Fig. 7(a). Its mathematical expression reads:

$$\sigma = \begin{cases} \sigma_{\max} \dfrac{g_{\mathrm{n}}}{g_{\mathrm{c}}} \dfrac{27}{4} \left[1 - 2\dfrac{g_{\mathrm{n}}}{g_{\mathrm{c}}} + \left(\dfrac{g_{\mathrm{n}}}{g_{\mathrm{c}}} \right)^2 \right], & \text{if } \ 0 < \dfrac{g_{\mathrm{n}}}{g_{\mathrm{c}}} < 1, \\ 0, & \text{if } \ \dfrac{g_{\mathrm{n}}}{g_{\mathrm{c}}} \geq 1, \end{cases} \tag{1}$$

where we recognize that the shape of the CZM is determined by only two parameters, namely the peak cohesive traction, $\sigma_{\max}$, and the critical crack opening corresponding to complete decohesion, g_{c}.

The latter is a bilinear CZM proposed in [7], see also Fig. 7(b) for its graphical visualization. Its mathematical expression reads:

$$\sigma = \begin{cases} K g_{\mathrm{n}}, & \text{if } 0 < g_{\mathrm{n}} \leq \dfrac{\sigma_{\max}}{K}, \\ \sigma_{\max} - \left(g_{\mathrm{n}} - \dfrac{\sigma_{\max}}{K} \right) \dfrac{\sigma_{\max}}{g_{\mathrm{c}} - \sigma_{\max}/K}, & \text{if } \dfrac{\sigma_{\max}}{K} < g_{\mathrm{n}} \leq g_{\mathrm{c}}, \\ 0 & \text{if } g_{\mathrm{n}} > g_{\mathrm{c}}, \end{cases} \tag{2}$$

where we note that, in this case, we need to identify three model parameters: the peak stress $\sigma_{\max}$, the initial stiffness, K, and the critical opening, $g_{\mathbf{c}}$.

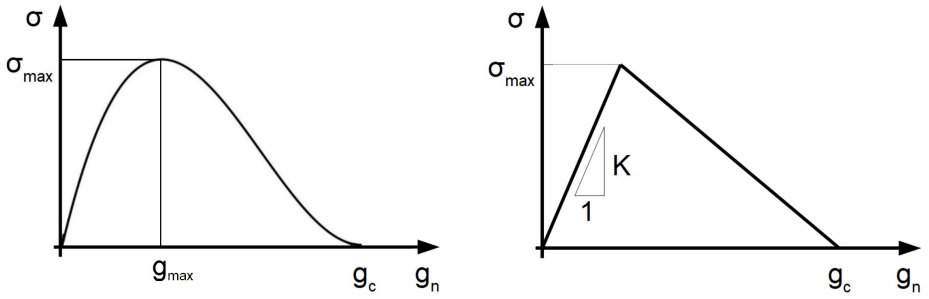

(a) Polynomial CZM (b) Bilinear CZM

Figure 7: The cohesive zone models herein considered for the mathematical description of nonlinear crack growth.

4. Parameters' identification procedure

Parameters' identification of nonlinear fracture mechanics models is a research topic that has received a great attention from the scientific community. In the case of linear elastic material behaviour for the bulk, the CZM parameters have been derived from experimental stress-strain data under the assumption of a general shape for the CZM and a predefined Mode I crack path in [8]. Later, the same approach has been explored in [9] for dynamic fracture events. Other attempts to indentify CZM parameters for adhesive interfaces embedded between linear-elastic materials have been proposed in [10, 11, 12]. In particular, it is remarkable to recall that a gradient-based optimization procedure was applied in [11, 12] to local and global experimental data obtained by digital image correlation. The issue of CZM parameters' identification

from local experimental measurements acquired by digital image correlation in the case of a simultaneous occurrence of nonlinear fracture and plasticity has been discussed in [13, 14].

Overall, the majority of those studies suggest that the shape of the CZM can play a substantial role in the accurate reproduction of the fracture process, which is an observation in line with theoretical arguments in [15]. In this regard, a direct identification of the CZM including its shape based on experimental data could be made according to the method proposed in [16] and relying on information gathered from the application of the digital image correlation technique to assess crack mouth opening displacements, and the fibre Bragg grating sensors to identify the fracture process zone development phase. For the application of that technique to the present problem, according to the authors' experience, digital image correlation could be applied in remote to SEM images acquired during loading, even without the need of painting a speckle pattern onto the specimen surface. This is because, at that observation scale, the surface specimen naturally presents a random grey-scale pattern, see Fig. 5, that can be used to statistically identify the displacements associated to each pixel. On the other hand, the application of fibre Bragg sensors could present some issues in terms of size and connection inside the SEM. Standard fibre Bragg sensors have also a diameter of about 100 μm, which is too big to achieve a sufficiently fine spatial resolution in the present application, see the scalebar in Fig. 5 to appreciate the length scales involved in the fracture process. Therefore, special fibre Bragg sensors should be used.

Another alternative approach could be based on the identification of the CZM relation based on full-field displacements only, an information that can be experimentally determined using digital image correlation. This very promising approach proposed in [17] was also adopting a spline curve with up to 8 knot points to mathematically describe the CZM law to be identified, in order to avoid restrictive assumptions on its shape. Regarding the bulk material response, on the other hand, they considered a homogeneous, isotropic and linear elastic constitutive relation. To apply the method in [17] to the present problem, it has to be remarked that the introduction of an elastoplastic material response with hardening for the bulk would introduce another nonlinearity in the identification procedure, in addition to cohesive fracture. Therefore, the corresponding identification procedure in [17] is not straightforward to be generalized. Its ability to converge to a unique set of material parameters should also be carefully investigated, due to nonconvexity issues. Comparisons with these alternative techniques are therefore left for further investigation.

In the present case, due to the presence of two forms of material nonlinearity, *i.e.*, elasto-plasticity and cohesive fracture, the model parameters to be identified are three for the elasto-plastic model with hardening, plus two (for the polynomial CZM) or three (for the bilinear CZM).

The simultaneous identification of five or six model parameters is computationally demanding and, whenever is possible, it would be preferable to consider loading scenarios which lead to the occurrence of just one of the two nonlinearities, so that identification can be made on a reduced number of model parameters. In the present case, the uniaxial tensile test on unnotched specimens leads to the activation of

elasto-plasticity as the primary form of material nonlinearity, and therefore this problem can be analyzed first, to identify E, $\sigma_{\rm y}$, and H. Once the elasto-plastic model parameters are identified, the CZM parameters ($\sigma_{\max}$ and $g_{\rm c}$ for the polynomial CZM, or $\sigma_{\max}$, $g_{\rm c}$ and K for the bilinear CZM) can be identified in relation to tensile test data on a notched specimen.

Formally, in both cases, it is convenient to introduce a vector $\mathbf{p}$ of model parameters (for elasto-plasticity or for nonlinear fracture mechanics) which takes values in the parameter space $\mathcal{P}$, containing all the admissible values for $\mathbf{p}$. We claim that the parameter vector $\mathbf{p}$ is not admissible if the simulation leads to results with no physical meaning. Therefore, the feasible set $\mathcal{P}$ takes also into account physical or mathematical restrictions onto the model parameters. For each value of $\mathbf{p}$, the objective function Φ that measures the mismatch between experimental (taken as reference) and the simulated (based on a discretized finite element model) force-displacement curves is computed. More specifically, let us define the residual error in the force level as $\Delta F_h(\mathbf{p}) = F_h^{\rm exp} - F_h^{\rm sim}(\mathbf{p})$, where $F_h^{\rm exp}$ and $F_h^{\rm sim}(\mathbf{p})$ denote the measured (experimental) and numerical (simulated) force, respectively, obtained for a given far-field imposed displacement indexed by h ($h = 1, \ldots, N$), where N is the number of imposed displacements. The objective cost Φ to be minimized is thus defined as

$$\Phi(\mathbf{p}) = \sqrt{\sum_{h=1}^{N} (\Delta F_h(\mathbf{p}))^2 q_h} \tag{3}$$

where q_h ($h = 1, \ldots, N$) are positive weights which can be set to give a priority for some selected force-displacement points. If the weights q_h are all equal to each other, then all the points in the force-displacement curve contribute with the same importance to the construction of the cost function Φ.

In the next subsections, the computation of the minimum of Φ over the feasible parameter set $\mathcal{P}$ is performed using two numerical algorithms for nonconvex optimization. For elasto-plasticity, the *gradient descent* algorithm with backtracking line search [18] is proposed. For fracture mechanics' model identification, on the other hand, *particle swarm optimization* (PSO) [19] is exploited.

4.1. Identification of elasto-plastic parameters

As discussed in Sec. 4, elasto-plastic material parameters are collected in the vector $\mathbf{p} = (E, \sigma_{\rm y}, H)$ which can be identified separately from CZM parameters in relation to the uniaxial tensile test on an unnotched specimen. The feasible domain for the parameters $E, \sigma_{\rm y}, H$ is defined based on the following physical constraints:

$$\mathcal{P} = \{E, \quad \sigma_{\rm y}, \quad H \mid E > 0, \quad \sigma_{\rm y} > 0, \quad H > 0\}. \tag{4}$$

The discretized finite element model of the specimen requires considering standard elasto-plastic plane stress Q4-finite elements available in the finite element analysis programme FEAP [20]. The gradient descent method outlined in Algorithm 1 searches iteratively the minimum of the cost function Φ following, at each iteration, the negative gradient direction.

The algorithm is initialized with a guess set of parameters used as starting point, $\mathbf{p}^{(0)} \in \mathcal{P}$. For this case, since the test leads to a uniform stress state in the specimen, we can simply compute the stress-strain curve from the experimental force-displacement data (the average ones over 10 realization of the test) and use it to provide an initial estimate for $\mathbf{p}^{(0)}$. Alternatively, totally arbitrary initial values can be considered. In the sequel, to show the capability of the identification algorithm to work also with initial values quite far from the optimal ones, we estimate the initial value for the Young's modulus $E = 1000$ MPa and for the yield stress $\sigma_{\mathrm{y}} = 2.5$ MPa from experimental data, as the slope of the stress-strain curve in the elastic regime and the stress level corresponding to the departure from linearity, respectively. On the other hand, the hardening modulus is set equal to $H = 100$ MPa, which is far from an initial guess based on the slope of the experimental stress-strain curve in the plastic regime, which would suggest a value one order of magnitude lower.

At each iteration k, an approximation of the gradient $\nabla\Phi_{\mathrm{i}}^{(k)}$ of Φ with respect to $\mathbf{p}$ is computed (see Algorithm 1, line 2) using the central finite difference formula:

$$\nabla\Phi_{\mathrm{i}}^{(k)} = \frac{\partial\Phi}{\partial p_{\mathrm{i}}} \backsimeq \frac{1}{2\Delta p_{\mathrm{i}}}[\Phi(p_{\mathrm{i}}^{(k-1)} + \Delta p_{\mathrm{i}}) - \Phi(p_{\mathrm{i}}^{(k-1)} - \Delta p_{\mathrm{i}})] \tag{5}$$

where $p_{\mathrm{i}}^{(k-1)}$ is the i-th component of the vector $\mathbf{p}^{(k-1)}$, with $\mathbf{p}^{(k-1)}$ denoting the value of the vector $\mathbf{p}$ at the (previous) $(k-1)$-th iteration of the algorithm, and Δp_{i} is a small variation of the i-th component of $\mathbf{p}$ around $p_{\mathrm{i}}^{(k-1)}$. For a fixed value of $\mathbf{p}$, the cost function is computed through Eq. (3), where the vector $F_h^{\mathrm{sim}}(\mathbf{p})$ contains the predicted value of the force for each imposed displacement step.

Then, the parameter vector $\mathbf{p}^{(k)}$ is updated (Algorithm 1, line 4), moving $\mathbf{p}^{(k-1)}$ in the direction of the negative gradient $\nabla\Phi_{\mathrm{i}}^{(k)}$ scaled by a positive constant t, which determinates the maximum amount to move along the direction of the negative gradient. The scaling factor t is chosen according to the *backtracking line search* criterion (Algorithm 1, line 3) [18, Chapter 3] sketched in Algorithm 2. The main idea of any *line search* criterion is to try different values of $t \in (0, 1]$, which correspond to different possible updates $\mathbf{p}^{\mathrm{trial}}$ of $\mathbf{p}$ (Algorithm 2, line 4) until a stopping criterion is reached (Algorithm 2, line 3). Note that the parameter under test, $\mathbf{p}^{\mathrm{trial}}$, is considered only if it belongs to the feasible parameter set $\mathcal{P}$ (Algorithm 2, lines 5 - 7). In this work, the parameters α and β characterizing the backtracking line search algorithm are both set equal to 0.5.

Table 1 shows the optimal value of the parameters entering the vector $\mathbf{p}$ obtained by running the Algorithm 1, along with the initial guess $\mathbf{p}^{(0)}$. The CPU time required to run Algorithm 1 is around 40 minutes. Convergence is reached after 110 iterations.

The cost function is calculated with or without using different weights q_h. These weights are used to improve the interpolation of the linear part, which contains less experimental points than the other part. Thus, a higher weight is given to the points in the linear regime by computing q_h as the ratio between the number of experimental points in the nonlinear plastic branch and the number of data points in the linear-

Algorithm 1: Gradient descent method

Inputs: initial guess $\mathbf{p}^{(0)} \in \mathcal{P}$; maximum number of iterations $k_{\max}$; tolerance ϵ.

Output: parameter vector $\mathbf{p}^{\text{opt}}$ minimizing Φ.

for $k = 1, 2, \ldots$ **do**
  compute gradient $\nabla\Phi^{(k)}$ (Eq. (5));
  choose scaling factor t via backtracking line search (Algorithm 2);
  set $\mathbf{p}^{(k)} \leftarrow \mathbf{p}^{(k-1)} - t\nabla\Phi^{(k)}$;
  until: $\left\|\nabla\Phi^{(k)}\right\|_2^2 \geq \epsilon$ **and** $k < k_{\max}$;
end for
set $\mathbf{p}^{\text{opt}} \leftarrow p^{(k)}$.

Algorithm 2: Backtracking line search

Input: gradient $\nabla\Phi^{(\mathrm{k})}$ at $\mathbf{p}^{(k-1)}$; parameters $\alpha \in (0, \frac{1}{2}]$ and $\beta \in (0, 1)$

Output: scaling parameter t

$t = 1$;
$\bar{\mathbf{p}} = \mathbf{p}^{(\mathrm{k}-1)}$;
while $\Phi(\bar{\mathbf{p}}) > \Phi(\mathbf{p}^{(k-1)}) - \alpha t \left\|\nabla\Phi^{(\mathrm{k})}\right\|_2^2$ **do**
  set $\mathbf{p}^{\text{trial}} \leftarrow \mathbf{p}^{(k-1)} - t\nabla\Phi^{(\mathrm{k})}$;
  if $\mathbf{p}^{\text{trial}} \in \mathcal{P}$ **then**
    set $\bar{\mathbf{p}} \leftarrow \mathbf{p}^{\text{trial}}$;
  end if
  update $t \leftarrow \beta t$;
end while

elastic branch. The evolution of the predictions provided by the gradient descent method as a function of the number of iterations, with or without uniform weights, is shown in Fig. 8. The use of higher weights for the data points in the linear regime (thus increasing the influence of these data in the evaluation of the cost function Φ) leads to a better approximation of the linear-elastic part of the stress-strain curve with an identified Young's modulus higher than the initial one. We also notice a much faster convergence of H and σ_{y} to the optimal values after just about 30 iterations.

Based on the identified optimal elasto-plastic parameters, the numerically predicted stress-strain curve matches very closely the average experimental one, see Fig. 9. Information on the experimental scatter can

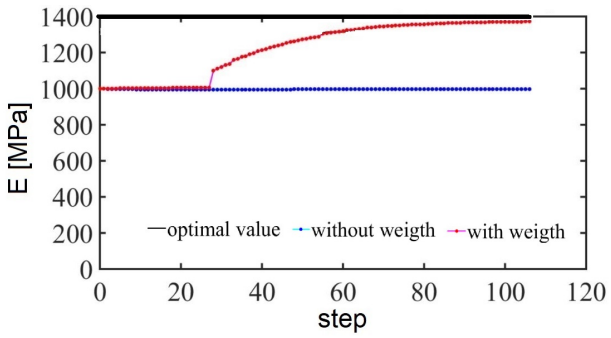

(a)

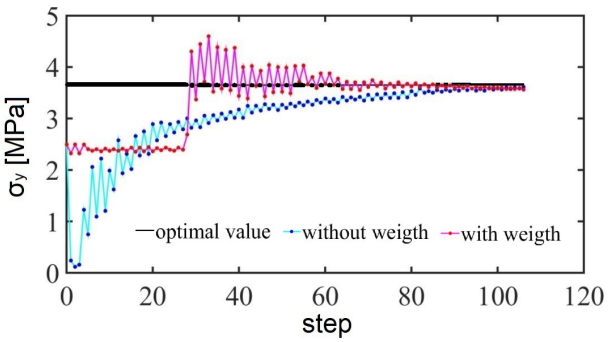

(b)

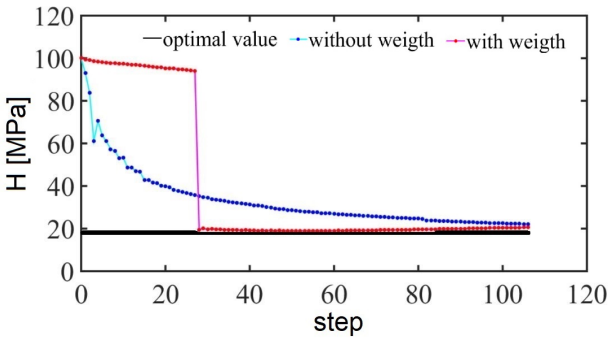

(c)

Figure 8: Elasto-plastic parameters' identification vs. number of iteration steps: (a) Young modulus, E; (b) yield stress, σ_{y}; (c) hardening coefficient, H. Results of the gradient-descent method using non-uniform weights are shown in purple; using homogenous weights in blue. Optimal identified parameters are shown in black.

$\mathbf{p}$	Initial guess	Gradient descent method results with nonuniform weights
E	1000 MPa	1367 MPa
σ_y	2.5 MPa	4.05 MPa
H	100 MPa	17.70 MPa

Table 1: Gradient descent method: initial and identified elasto-plastic model parameters.

also be appreciated from the grey region which corresponds to the envelope of all the 10 repetitions of the test. The reproducibility of experimental response is very high. At much smaller scales than that of the present tests, as for MEMS or NEMS, the geometrical and material imperfections have a much higher effect on the reproducibility of the mechanical results and on the experimental scatter [21].

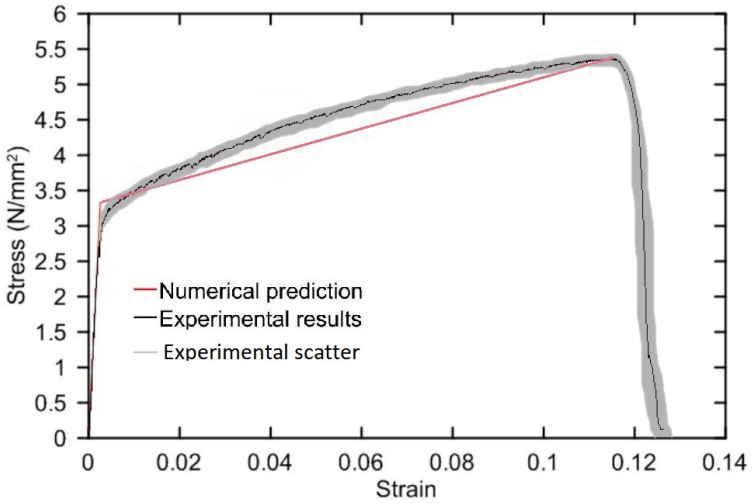

Figure 9: Comparison between the average experimental stress-strain curve (over 10 realizations) of the unnotched specimen and the simulated one using the optimally identified elasto-plastic model parameters. The envelope of the experimental curves is shown in grey.

4.2. Identification of nonlinear fracture mechanics parameters

The identification of CZM parameters has to be performed by taking the experimental results on a notched specimen as a reference response to match.In this case, we consider the average experimental data over 10 realization of the uniaxial tensile test on the notched specimen with $a_0 = 0.45$ mm notch size.

The finite element model requires plane stress Q4 elasto-plastic finite elements for the continuum and zero-thickness interface finite elements to simulate the growth of the material discontinuity caused by cohesive crack propagation. Since the geometry of the problem and the boundary conditions promote a Mode I crack growth along a pre-defined straight path, it is possible to take advantage from this information and

insert interface finite elements along the mid-span cross-section of the specimen from the beginning of the simulation, avoiding remeshing operations at each loading step (see Fig. 10).

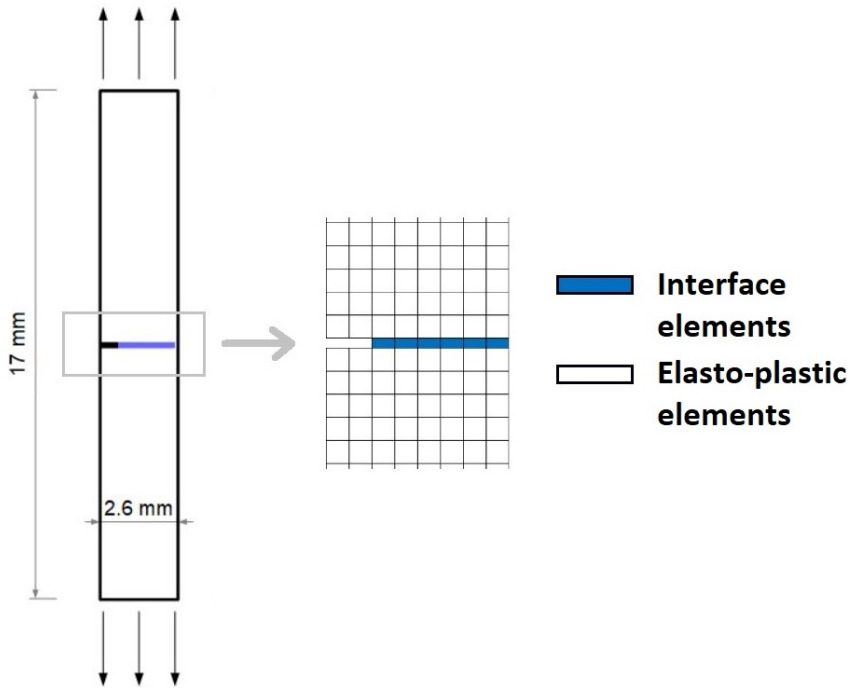

Figure 10: Geometry of a notched specimen and detail of the FE mesh at the notch-tip.

To formulate the CZM parameters' identification as an optimization problem, it is convenient to stack the CZM parameters to be identified in a vector $\mathbf{p}$ defined as:

$$\mathbf{p} = [\sigma_{\max}, g_c] \qquad \text{for the polynomial CZM, see Eq. (1),}$$

$$\mathbf{p} = [\sigma_{\max}, g_c, K] \qquad \text{for the bilinear CZM, see Eq. (2).}$$

Due to the fact that the presence of a notch leads to a non homogenous stress-field throughout the specimen, the simulated global force-displacement curve that should match the experimental one is a nonlinear implicit function of the CZM and of the elasto-plastic material model parameters. Therefore, identification requires the exploration of a large set of admissible values, solve the corresponding nonlinear FE problem to compute the simulated force-displacement curve, and finally identify the optimal set leading to the best match with the experimental results (global minimum of the cost function). An automatized robust and efficient identification procedure is therefore required.

In this regard, it has been found that the application of the gradient descent algorithm, successfully used for the elasto-plastic material model identification, presents some drawbacks when applied to CZM parameters identification. Specifically, two main issues have been reported from the tests:

- For many different initial guesses $\mathbf{p}^{(0)}$, the solution of Algorithm 1 remains in the neighbourhood of

$\mathbf{p}^{(0)}$. This is due to the non convexity of the cost function Φ, which causes the algorithm to trap in a local minimum.

- The convergence speed is in general very slow. This is a well known problem of gradient-based optimization algorithms, and it is due to the fact that the gradient tends to zero when the parameter vector $\mathbf{p}^{(k)}$ approaches a (local) minimum. This makes the update of the parameter $\mathbf{p}$ small (see Algorithm 1, line 4).

In order to overcome these drawbacks, particle swarm optimization (PSO), which is a derivative-free algorithm, is herein proposed to minimize the cost function Φ. The PSO is based on swarm of particles which explore the parameters domain $\mathcal{P}$, seeking for the minimum of Φ. This method, along with simulated annealing, are widely applied to structural and material optimization problems, see e.g. [22, 23, 24, 25] among many others. The PSO approach is outlined in Algorithm 3. The components of the optimization vector $\mathbf{p}$ define the coordinates of the particle. The algorithm is initialized by randomly generating M particles in the domain $\mathcal{P}$ (Algorithm 3, line 2). A randomly generated velocity vector $\mathbf{v}_i$ is associated to each particle (Algorithm 3, line 5). At each iteration k of the PSO algorithm, each particle updates its position in the space $\mathcal{P}$ (Algorithm 3, lines 10 and 11) based on: (i) its previous velocity $\mathbf{v}_i^{(k-1)}$ (inertia); (ii) its own best known position p_i^{opt} in the search-space $\mathcal{P}$ (local knowledge); (iii) the swarm's best known position $\mathbf{p}_{\text{G}}^{\text{opt}}$ (global knowledge). The algorithm's parameters W, C_{L} and C_{G} weight the influence of these three contributions in the update of the particle's velocity $\mathbf{v}_i^{(k)}$. The local p_i^{opt} and global $\mathbf{p}_{\text{G}}^{\text{opt}}$ best positions are updated at each iteration (Algorithm 3, lines 15 - 21). The algorithm terminates when the maximum number of iterations $k_{\max}$ is reached.

The application of PSO to the identification of the polynomial CZM parameters requires the definition of the feasible set $\mathcal{P}$, based on preliminary information that can be gained from experimental data gathered from the tensile stage and from SEM images:

$$\mathcal{P} = \{\sigma_{\max}, \quad g_{\text{c}} \mid \ 3 \text{ MPa } < \sigma_{\max} < \ 15 \text{ MPa }, 0.01 \text{ mm } < g_{\text{c}} < \ 0.5 \text{ mm } \}.$$

Algorithm 3 is run for $k_{\max} = 300$ iterations and $M = 30$ particles, with parameters $W = 0.5$, $C_{\text{L}} = 0.2$ and $C_{\text{G}} = 0.1$. The optimally identified polynomial CZM parameters are $\sigma_{\max} = 8.60$ MPa and $g_{\text{c}} = 0.19$ mm. The algorithm terminates after just 18 iterations, when all the particles are concentrated in a small area. Fig. 11 shows the evolution of the estimated parameters for some representative iterations. Circles depict the particles' position and their radii are proportional to the value of the cost function Φ computed at the particles' position. For each particle, its velocity is also displayed as a black vector. The red filled circle represents the swarm's best position, which provides the current global optimum. The identified optimal set of parameters leads to a very good agreement between the average experimental force-displacement curve and the numerically simulated one for the specimen with a notch size of 0.45 mm, see

Algorithm 3: Particle swarm optimization algorithm.

Input: number of particles M, number of iterations $k_{\max}$, algorithm's parameters W, C_{L} and C_{G}.

Output: parameter vector $\mathbf{p}_{\mathrm{G}}^{\mathrm{opt}}$ minimizing Φ.

—— **Initialization** ——

for all $i = 1 : M$ **do**
  generate random particle $\mathbf{p}_i^{(0)}$ in $\mathcal{P}$;
  compute the cost $\Phi(\mathbf{p}_i^{(0)})$;
  set local optimizer $\mathbf{p}_i^{\mathrm{opt}} \leftarrow \mathbf{p}_i^{(0)}$;
  generate random particle's velocity vector $\mathbf{v}_i^{(0)}$;
end for
set global optimizer $\mathbf{p}_{\mathrm{G}}^{\mathrm{opt}} \leftarrow \arg\min_{\mathbf{p}_i^{(0)}} \Phi(\mathbf{p}_i^{(0)})$;

—— **Iterations** ——

for $k = 1, 2, \ldots, k_{\max}$ **do**
  for all $i = 1 : M$ **do**
    update particle's velocity $\mathbf{v}_i^{(k)} \leftarrow W\mathbf{v}_i^{(k-1)} + C_{\mathrm{L}}(\mathbf{p}_i^{\mathrm{opt}} - \mathbf{p}_i^{(k-1)}) + C_{\mathrm{G}}(\mathbf{p}_{\mathrm{G}}^{\mathrm{opt}} - \mathbf{p}_i^{(k-1)})$;
    update particle's position $\mathbf{p}_i^{(k)} \leftarrow \mathbf{p}_i^{(k-1)} + \mathbf{v}_i^{(k)}$;
    if $\mathbf{p}_i^{(k)} \notin \mathcal{P}$ **then**
      relocate randomly $\mathbf{p}_i^{(k)}$ in $\mathcal{P}$;
    end if
    compute the cost $\Phi(\mathbf{p}_i^{(k)})$;
    if $\Phi(\mathbf{p}_i^{(k)}) < \Phi(\mathbf{p}_i^{\mathrm{opt}})$ **then**
      update local optimizer $\mathbf{p}_i^{\mathrm{opt}} \leftarrow \mathbf{p}_i^{(k)}$;
      if $\Phi(\mathbf{p}_i^{(k)}) < \Phi(\mathbf{p}_{\mathrm{G}}^{\mathrm{opt}})$ **then**
        update global optimizer $\mathbf{p}_{\mathrm{G}}^{\mathrm{opt}} \leftarrow \mathbf{p}_i^{(k)}$;
      end if
    end if
  end for
end for

Fig. 12(a).

When those CZM parameters are used to simulate the experimental force-displacement curve for the specimen with a notch size of 0.80 mm, such a validation step shows that the simulated curve is still very

close to the experimental one up to the peak force, see Fig. 12(b), thus capturing the lower maximum force level that can be withstand by that specimen. Moreover, it also predicts a smaller displacement at failure, consistently with the experimental evidence. On the other hand, the numerical simulation is slightly underestimating the force level in the post-peak regime.

The PSO algorithm is also used to estimate the parameters of the bilinear three-parameter CZM in Eq. (2). This CZM allows the control of the initial stiffness of the traction-separation relation by varying the ratio $\sigma_{\max}/K$, while this was not modifiable in the polynomial CZM. Again, the parameters $\sigma_{\max}$, $g_{\rm c}$, and K of the bilinear CZM can be estimated based on experimental data gathered from tests on the 0.45 mm notched specimen. The feasible set for the bilinear CZM parameters is:

$$\mathcal{P} = \{\sigma_{\max}, \quad g_{\rm c}, \quad K \mid$$
$$8 \text{ MPa} < \sigma_{\max} < 20 \text{ MPa}; \quad 0.001 \text{ mm} < g_{\rm c} < 0.1 \text{ mm}; \quad 10^3 \text{MPa/mm} < K < 10^4 \text{ MPa/mm}; \quad K \geqslant \sigma_{\max}/g_{\rm c}\}.$$

The feasibility condition $K \geqslant \sigma_{\max}/g_{\rm c}$ is enforced to avoid a shape of the CZM which is physically not admissible, i.e., to guarantee a critical opening for complete decohesion, $g_{\rm c}$, larger than the crack opening corresponding to the peak cohesive traction.

Algorithm 3 is run for $k_{\max} = 300$ iterations and $M = 30$ particles, with parameters $W = 0.5$, $C_{\rm L} = 0.2$ and $C_{\rm G} = 0.1$. The optimally identified bilinear CZM parameters are $\sigma_{\max} = 13.3$ MPa, $g_{\rm c} = 0.07$ mm, $K = 6610$ MPa/mm. The algorithm terminates after just 17 iterations, when all the particles are concentrated in a small area. Fig. 13 shows the evolution of the identified parameters for some representative iterations of the algorithm. As for the polynomial CZM, circles depict the particles' positions and their radii are proportional to the value of the cost function Φ computed at the particles' position. For each particle, its velocity is also displayed as a black vector. The red filled circle represents the swarm's best position, which provides the current global optimum. These three diagrams superimposed to each other are shown in Fig. 14, to highlight the ability of the algorithm in exploring the values of the cost function in the surroundings of the current global optimum.

The force-displacement curve related to the optimal identified bilinear CZM for the 0.45 mm notch size specimen is shown in Fig. 12(a). It is worth noticing that, although the bilinear CZM is described by three parameters, its accuracy in reproducing the global experimental response is similar to that of the polynomial CZM. A similar agreement is noticed for the verification case on the 0.80 mm notch-size specimen, Fig. 12(b).

The evolution of the cost function Φ predicted from PSO for the two CZMs is compareteively shown in Fig. 15, which is a steady decreasing function of the number of PSO iterations.

In addition to the analysis of the goodness of fit of the global force-displacement curve, it is worth examining SEM images to the inspection the accuracy of the two identified CZMs in reproducing local qualities associated to crack growth, such as the critical crack opening, $g_{\rm c}$. In this regard, the value of the critical crack opening identified by the bilinear CZM is more physically sound than that related to the

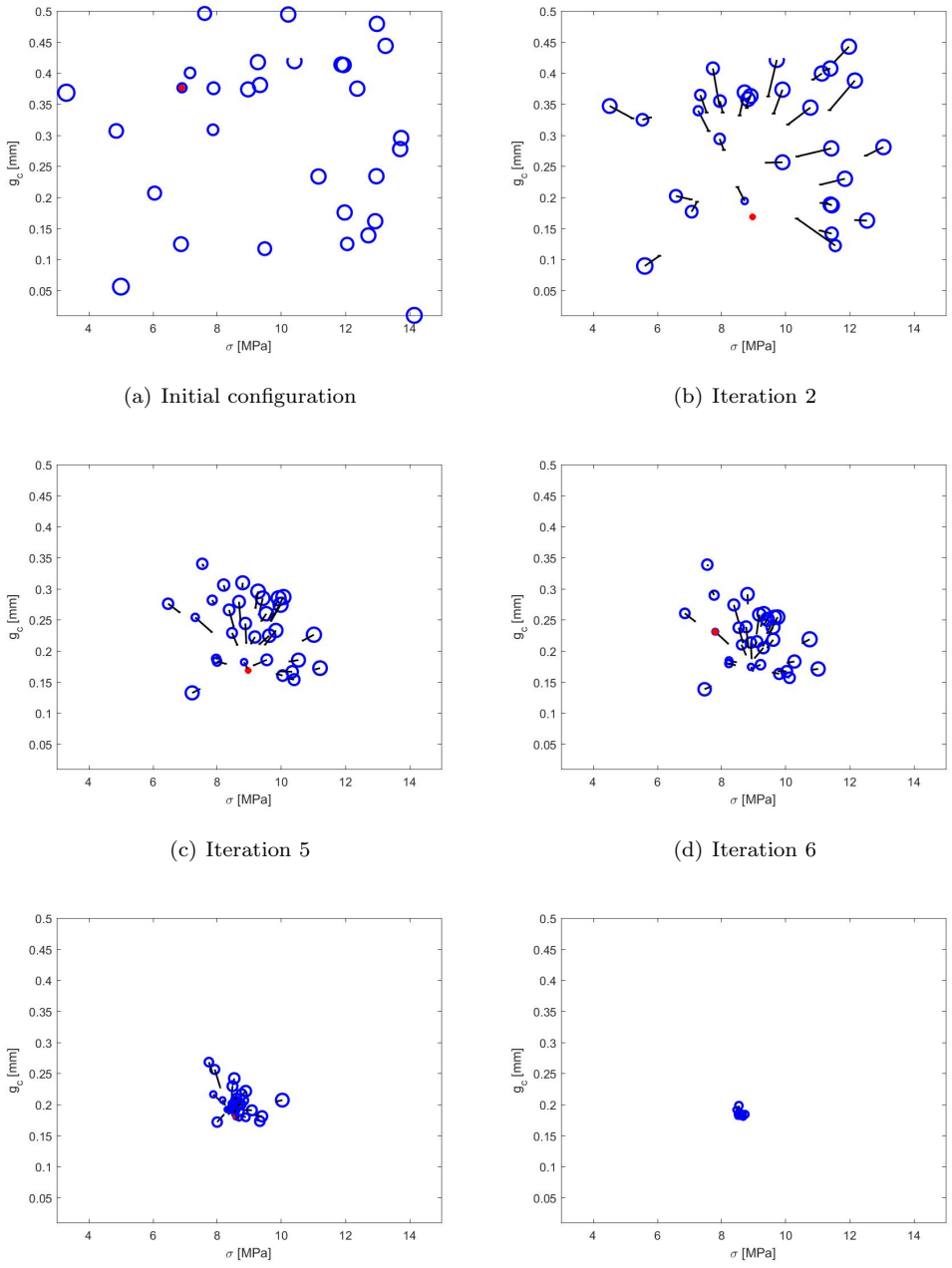

(a) Initial configuration

(b) Iteration 2

(c) Iteration 5

(d) Iteration 6

(e) Iteration 10

(f) Iteration 18

Figure 11: Most representative iterations of the PSO evolution applied to the identification of the polynomial CZM parameters.

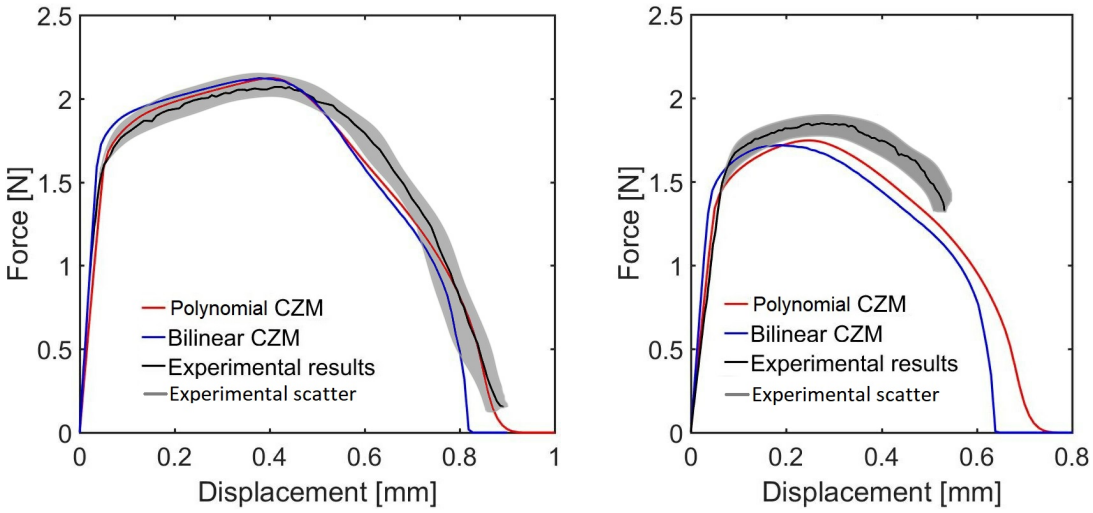

(a) Identification: 0.45 mm notched specimen

(b) Validation: 0.80 mm notched specimen

Figure 12: PSO optimization: comparison betweeen the simulated and the average experimental force-displacement curves, depending on the CZM and the notched specimen. Experimental data for the 0.45 mm notch size have been used to identify the model parameters, while the data for the 0.80 mm notch size have been considered for validation. The grey regions denote the envelope of the experimental results over 10 repetitions of the test.

identified polynomial CZM. SEM images reported in Sec. 2 (Fig. 5) suggest in fact a value for the critical crack opening of the order of about few tens of micrometers, not hundreds of micrometers as obtained from the polynomial CZM.

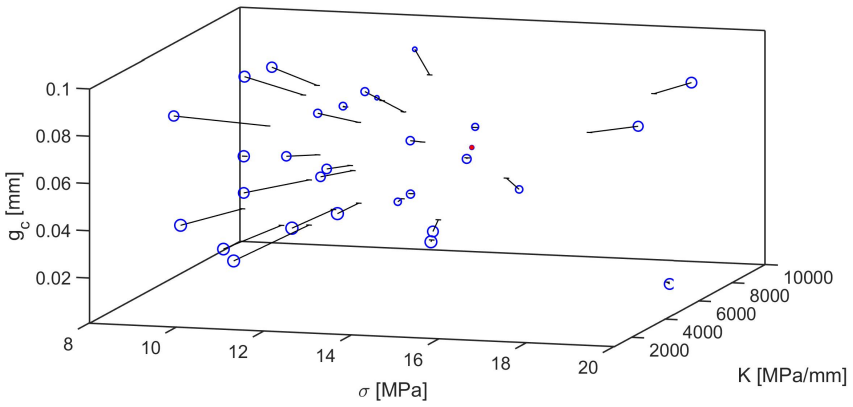

(a) Initial values

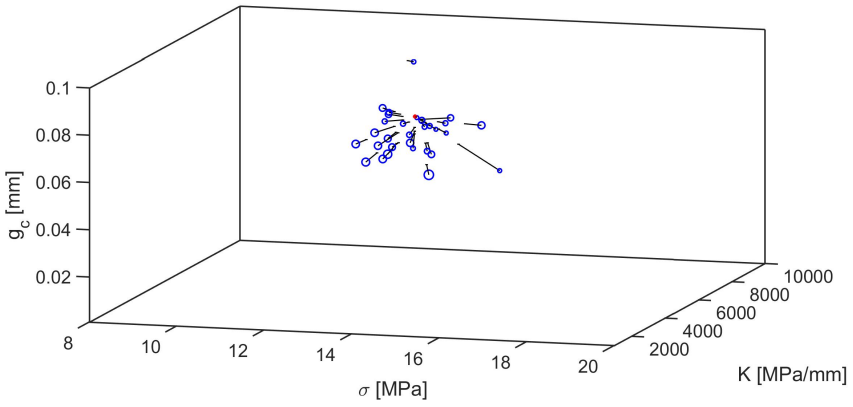

(b) Iteration 6

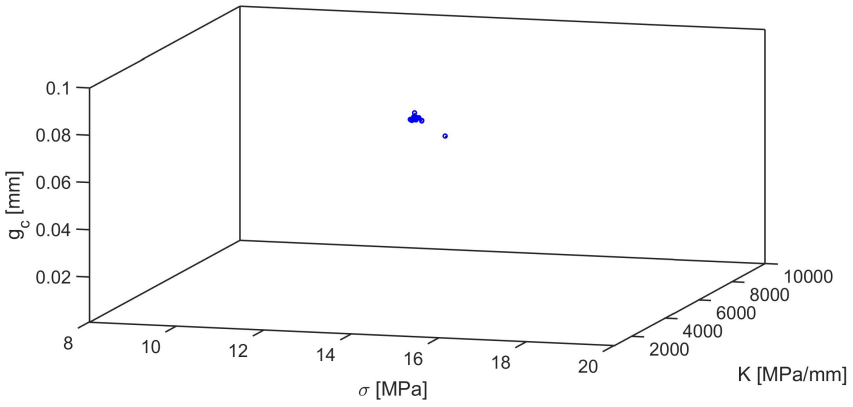

(c) Iteration 17

Figure 13: 3D representation of the identified bilinear CZM parameters based on PSO: (a) iteration 0 (initial configuration); (b) iteration 6; (c) iteration 17.

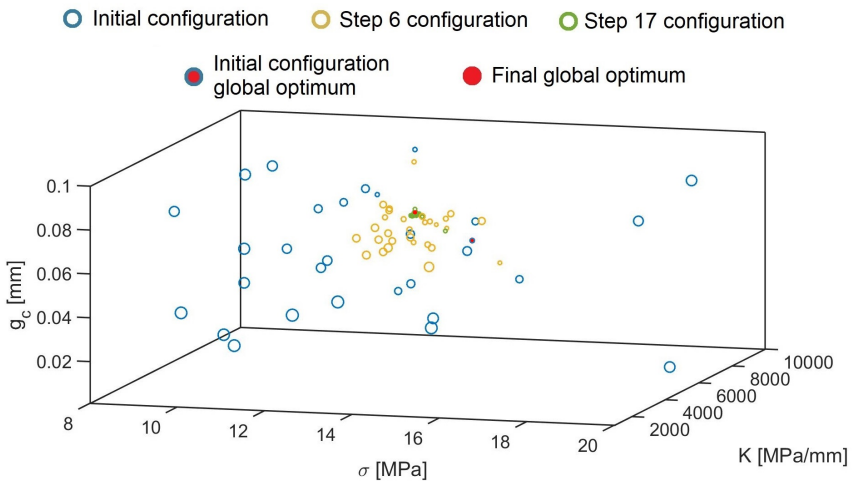

Figure 14: Summary of the PSO iterations for the identification of the bilinear CZM parameters.

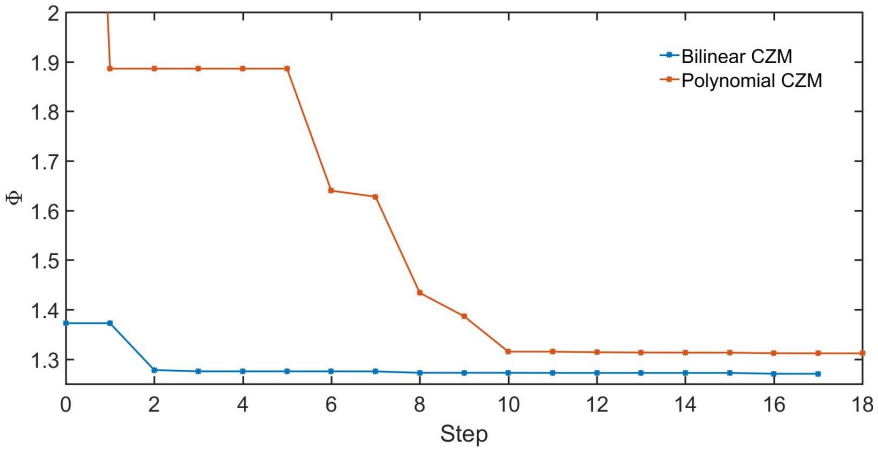

Figure 15: Evolution of the cost function Φ during PSO iterations for the two CZMs herein considered.

5. Discussion and conclusion

A robust optimization procedure for the identification of elasto-plastic and cohesive zone model (CZM) parameters has been proposed in relation to silver-plated copper material used for busbars and wires in photovoltaic modules. The procedure requires the experimental determination of global force-displacement curves from uniaxial tensile tests on unnotched and notched busbars. In addition to global measures, we have also recommended to acquire local measurements such as the crack-tip deformation using in situ SEM imaging. The elasto-plastic material parameters based on von Mises plasticity with isotropic hardening have been identified using experimental data on unnotched specimens by a gradient descent method with back-tracking line search. For its best performance, the use of non-uniform weights has been suggested, especially to better reproduce the linear-elastic branch of the force-displacement curve where less experimental data points are available as compared to those recorded in the hardening phase.

Once elasto-plastic material parameters are identified, force-displacement curves on notched specimens can be used to identify the remaining CZM parameters. In such a case, the simultaneous occurrence of plasticity and cohesive fracture renders the problem highly nonlinear and nonconvex. Hence, to overcome the drawbacks of gradient-based optimization algorithms, we exploited the use of particle swarm optimization. Its application allows a fast convergence to the procedure and the identification of two model parameters (for the polynomial CZM) or three model parameters (for the bilinear CZM), replicating with good accuracy the experimental global force-displacement curves of notched samples. However, a closer look at the identified parameters of the two CZMs shows that the identified Mode I critical crack opening for the polynomial CZM is much larger than what expected from local measurement from SEM images. The same value for the bilinear CZM, on the other hand, is much smaller and more consistent with SEM images. This confirms that the shape of the CZM matters in reproducing not only global quantities, but also local features of crack growth. Therefore, for the present material, a bilinear CZM where the initial stiffness of the traction-separation relation can be selected intependently from the critical crack opening is recommended to be used in numerical simulations.

Further research on this topic could require the extension of the optimization algorithms to Mixed Mode crack growth scenarios and cyclic loading. At present, since the busbar is predominatly subjected to axial deformation with crack growth under a predominant Mode I deformation, this issue has been left for further investigation.

Regarding cyclic loading, it has been shown in [4] that the unloading path of the stress-strain curve for unnotched specimens is affected by material damage, with reloading paths not coincident with the unloading ones for repeated cycles. This issue increases the complexity and the number of elastoplastic material parameters to be introduced and then identified, in addition to the need of considering a damage evolution law to describe cyclic degradation effects. Therefore, the complexity of the material parameters

identification procedure significantly increases in its turn. Moreover, in the case of notched specimens, the description of unloading and reloading paths during the post-peak branch affected by crack growth and plasticity is expected to be even more complex to be described. A preliminary experimental test to show the cyclic material response for the notched specimen with 0.80 mm notch size is shown in Fig.16. The shape of the hysteretic curves is changing depending on the initial point of unloading. Moreover, repeated cycles do not lead to completely overlapping hysteretic curves, implying material degradation effects due to repeated cycles as for unnotched specimens. To model such a behavior, the unloading and reloading paths of the cohesive zone models should also be introduced, including an assumption on the cohesive zone model parameters degradation law, see e.g. [26, 27] for possible modelling strategies. This would dramatically increase the number of parameters to be identified by the optimization procedure and therefore this task has also been left for future research.

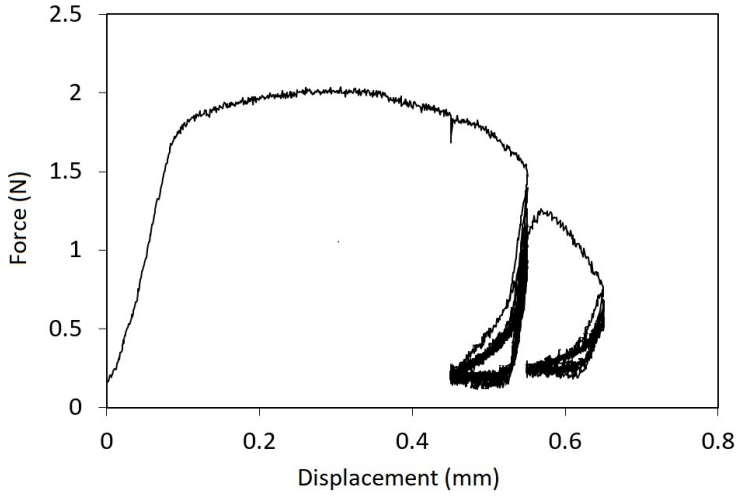

Figure 16: Force-displacement curve for a specimen with $a_0 = 80\,\mu$m. In the post-peak branch, repeated cyclic loading paths under displacement control have been imposed to show the complexity of the hysteretic loops and also their change over cycles due to material damage.

Acknowledgments

Support of the European Research Council to the H2020 ERC Proof of Concept 2016 grant PHYSIC – Photovoltaics with superior crack resistance (GA n. 737447) is gratefully acknowledged.

References

[1] M. Paggi, I. Berardone, A. Infuso, and M. Corrado. Fatigue degradation and electric recovery in silicon solar cells embedded in photovoltaic modules. *Scientific reports*, 4:04506, 2014.

[2] U. Eitner. *Thermomechanics of Photovoltaic Modules*. Ph.D. Thesis, Martin Luther University, Halle-Wittenberg, 2011.

[3] M. Paggi, S. Kajari-Schröder, and U. Eitner. Thermomechanical deformations in photovoltaic laminates. *The Journal of Strain Analysis for Engineering Design*, 46(8):772–782, 2011.

[4] C. Borri, M. Gagliardi, and M. Paggi. Fatigue crack growth in silicon solar cells and hysteretic behaviour of busbars. *Solar Energy Materials and Solar Cells*, 181:21–29, 2018.

[5] M. Köntges, G. Oreski, U. Jahn, M. Herz, P. Hacke, K.-A. Weiss, G. Razongles, M. Paggi, D. Parlevliet, T. Tanahashi, and R.H. French. *Assessment of Photovoltaic Modules in the Field*. Technical report of the International Energy Agency, IEA-PVPS T13-09:2017, 2017.

[6] V. Tvergaard. Effect of fibre debonding in a whisker-reinforced metal. *Materials science and engineering: A*, 125(2):203–213, 1990.

[7] P.H. Geubelle and J.S. Baylor. Impact-induced delamination of composites: a 2d simulation. *Composites Part B: Engineering*, 29(5):589–602, 1998.

[8] Soonsung Hong and Kyung-Suk Kim. Extraction of cohesive-zone laws from elastic far-fields of a cohesive crack tip: a field projection method. *Journal of the Mechanics and Physics of Solids*, 51(7):1267 – 1286, 2003.

[9] Irene Arias, Jaroslaw Knap, Vijaya B. Chalivendra, Soonsung Hong, Michael Ortiz, and Ares J. Rosakis. Numerical modelling and experimental validation of dynamic fracture events along weak planes. *Computer Methods in Applied Mechanics and Engineering*, 196(37):3833 – 3840, 2007. Special Issue Honoring the 80th Birthday of Professor Ivo Babuška.

[10] L. Andena, M. Rink, and J.G. Williams. Cohesive zone modelling of fracture in polybutene. *Engineering Fracture Mechanics*, 73:2476–2485, 2006.

[11] N. Valoroso and R. Fedele. Characterization of a cohesive-zone model describing damage and de-cohesion at bonded interfaces. sensitivity analysis and mode-i parameter identification. *International Journal of Solids and Structures*, 47(13):1666 – 1677, 2010.

[12] R. Fedele, B. Raka, F. Hild, and S. Roux. Identification of adhesive properties in glare assemblies using digital image correlation. *Journal of the Mechanics and Physics of Solids*, 57(7):1003 – 1016, 2009.

[13] H. Tan, C. Liu, Y. Huang, and P.H. Geubelle. The cohesive law for the particle/matrix interfaces in high explosives. *Journal of the Mechanics and Physics of Solids*, 53(8):1892 – 1917, 2005.

[14] V. Richefeu, A. Chrysochoos, V. Huon, Y. Monerie, R. Peyroux, and B. Wattrisse. Toward local identification of cohesive zone models using digital image correlation. *European Journal of Mechanics - A/Solids*, 34:38 – 51, 2012.

[15] M. Paggi and P. Wriggers. A nonlocal cohesive zone model for finite thickness interfaces–Part I: mathematical formulation and validation with molecular dynamics. *Computational Materials Science*, 50(5):1625–1633, 2011.

[16] J. Xavier, J.R.A. Fernandes, O. Frazão, and J.J.L. Morais. Measuring mode i cohesive law of wood bonded joints based on digital image correlation and fibre bragg grating sensors. *Composite Structures*, 121:83–89, 2015.

[17] B. Shen and G.H. Paulino. Identification of cohesive zone model and elastic parameters of fiber-reinforced cementitious composites using digital image correlation and a hybrid inverse technique. *Cement and Concrete Composites*, 33:527–585, 2011.

[18] J. Nocedal and S.J. Wright. *Sequential quadratic programming*. Springer, 2006.

[19] M. Clerc. *Particle swarm optimization*, volume 93. John Wiley & Sons, 2010.

[20] O.C. Zienkiewicz and R.L. Taylor. *The finite element method: solid mechanics*, volume 2. Butterworth-heinemann, 2000.

[21] T. Pardoen, M.-S. Colla, H. Idrissi, B. Amin-Ahmadi, B. Wang, D. Schryvers, U.K. Bhaskar, and J.-P. Raskin. A versatile lab-on-chip test platform to characterize elementary deformation mechanisms and electromechanical couplings in nanoscopic objects. *Comptes Rendus Physique*, 17:485–495, 2016.

[22] F. Javidrad and M. Nazari. A new hybrid particle swarm and simulated annealing stochastic optimization method. *Applied Soft Computing*, 60:634 – 654, 2017.

[23] O. Begambre and J.E. Laier. A hybrid particle swarm optimization – simplex algorithm (psos) for structural damage identification. *Advances in Engineering Software*, 40(9):883 – 891, 2009.

[24] Ammar N. Hanoon, M.S. Jaafar, Farzad Hejazi, and Farah N.A. Abdul Aziz. Strut-and-tie model for externally bonded cfrp-strengthened reinforced concrete deep beams based on particle swarm optimization algorithm: Cfrp debonding and rupture. *Construction and Building Materials*, 147:428 – 447, 2017.

[25] X. Zhang, R.X. Gao, R. Yan, X. Chen, C. Sun, and Z. Yang. Multivariable wavelet finite element-based vibration model for quantitative crack identification by using particle swarm optimization. *Journal of Sound and Vibration*, 375:200 – 216, 2016.

[26] K.L. Roe and T. Siegmund. An irreversible cohesive zone model for interface fatigue crack growth simulation. *Engineering Fracture Mechanics*, 70:209–232, 2003.

[27] B. Gong, M. Paggi, and A. Carpinteri. A cohesive crack model coupled with damage for interface fatigue problems. *International Journal of Fracture*, 173:91–104, 2012.